
Article:
Eldridge, C., Spooner, N.J.C., McLean, A.G. et al. (5 more authors) (2023) Directional dark matter readout with a novel multi-mesh ThGEM for SF6 negative ion operation. Journal of Instrumentation, 18 (08). P08021. ISSN 1748-0221

https://doi.org/10.1088/1748-0221/18/08/p08021

Journal of Instrumentation

PAPER • **OPEN ACCESS**

Directional dark matter readout with a novel multi-mesh ThGEM for SF_6 negative ion operation

To cite this article: C. Eldridge *et al* 2023 *JINST* **18** P08021

Jinst

Published by IOP Publishing for Sissa Medialab

Received: *November 6, 2022*
Revised: *May 10, 2023*
Accepted: *June 12, 2023*
Published: *August 23, 2023*

Directional dark matter readout with a novel multi-mesh ThGEM for SF_6 negative ion operation

C. Eldridge,[a] N.J.C. Spooner,[a] A.G. McLean,[a,*] J. Burns,[b] T. Crane,[c] A.C. Ezeribe,[a] R.R. Marcelo Gregorio[a] and A. Scarff[a]

[a] *Department of Physics and Astronomy, University of Sheffield, South Yorkshire, S3 7RH, U.K.*
[b] *Science and Technology Facilities Council (STFC), Swindon, SN2 1SZ, U.K.*
[c] *AWE plc, Aldermaston, Reading, Berkshire, RG7 4PR, U.K.*

E-mail: ali.mclean@sheffield.ac.uk

Abstract: Direct searches for Weakly Interacting Massive Particle (WIMP) dark matter could greatly benefit from directional measurement of the expected induced nuclear recoils. Gas-based Time Projection Chambers (TPCs) offer potential for this, opening the possibility of measuring WIMP signals below the so-called neutrino floor but also of directional measurement of recoils induced by neutrinos from the Sun, for instance as proposed by the CYGNUS collaboration. Presented here for the first time are results from a Multi-Mesh Thick Gas Electron Multiplier (MM-ThGEM) using negative ion gases for operation with such a directional dark matter TPC. Negative ion drift gases are favoured for directionality due to their low diffusion characteristics. The multiple internal mesh structure is designed to provide a high gain amplification stage when coupled to future large area Micromegas, strip or pixel charge readout planes. Experimental results and simulations are presented of MM-ThGEM gain and functionality using low pressure pure CF_4, SF_6 and SF_6:CF_4 mixtures irradiated with alpha particles and ^{55}Fe x-rays. The concept is found to work well, providing stable operation with gains over 10^3 in pure SF_6.

Keywords: Dark Matter detectors (WIMPs, axions, etc.); Gaseous detectors; Micropattern gaseous detectors (MSGC, GEM, THGEM, RETHGEM, MHSP, MICROPIC, MICROMEGAS, InGrid, etc); Neutron detectors (cold, thermal, fast neutrons)

*Corresponding author.

https://doi.org/10.1088/1748-0221/18/08/P08021

2023 JINST 18 P08021

Contents

1 Introduction **1**

2 MM-ThGEM design and operating principles **3**

3 MM-ThGEM set-up and calibration **4**

4 MM-ThGEM collection field in CF_4 **5**
- 4.1 Experimental measurement of gain and energy resolution 6
- 4.2 CF_4 charge transport simulation in Garfield++ 7
- 4.3 Conclusions 11

5 MM-ThGEM collection field in SF_6 **11**
- 5.1 Experimental measurement of gain and energy resolution 11
- 5.2 SF_6 charge transport simulation in Garfield++ 12
- 5.3 Conclusions 13

6 MM-ThGEM amplification fields in SF_6 **13**
- 6.1 MM-ThGEM gain with equal amplification fields 14
- 6.2 MM-ThGEM gain dependence on amplification field 2 14
- 6.3 Extracting Townsend gas parameters 15
- 6.4 Conclusions 17

7 Transfer field **17**
- 7.1 Effect of the transfer field on gas gain 17
- 7.2 Transfer times 18
- 7.3 Conclusions 20

8 Ion feedback effect in SF_6 **20**

9 Operation of the MM-ThGEM in CF_4:SF_6 **23**

10 Conclusions **24**

2023 JINST 18 P08021

1 Introduction

The work described here concerns the operation of the Multi-Mesh Thick Gas Electron Multiplier (MM-ThGEM), first described in [1], operated for the first time in a low pressure, Negative Ion (NI), gas Time Projection Chamber (NITPC). This detector type is being studied to develop technology for the directional detection of Weakly Interacting Massive Particles (WIMPs). Such particles

are a potential candidate for Dark Matter (DM), a heretofore undetected type of matter which is believed to constitute 85% of the mass of the Universe [2]. Progress continues to be made in the field with the development of larger detectors capable of probing smaller interaction cross-sections primarily based on liquid noble gasses [3, 5], the basis being detection of energy transferred from nuclear recoils expected following WIMP-nucleus elastic scattering. However, apart from the DAMA/LIBRA claimed detection using annual modulation [4], now strongly constrained by COSINE-100 and other experiments using the same NaI target [6], no WIMP signal detection has been declared. Meanwhile, the sensitivity of current generation experiments is approaching the so-called neutrino floor, a background of nuclear recoils from coherent scattering of neutrinos mainly from the Sun. Gas TPCs offer a potential of transcending this floor by measuring the direction of the WIMP-induced recoils. The motion of our Solar System through the assumed galactic WIMP distribution means this signal can not easily be mimicked by recoils from the neutrino, or neutron, backgrounds which have different angular distributions.

Directional recoil signals are obtained in gas TPCs by reconstructing the ionising tracks produced following drift of the charge to a pixelated, wire or xy strip readout. The DRIFT collaboration pioneered this idea with low background NITPCs [7] using multi-wire proportional chambers (MWPCs) with CS_2 typically at 40 Torr. There are a number of properties of Negative ion drift gasses that are advantageous for WIMP detection; there is less diffusion of charge carriers during the drift as compared to electron drift gasses, enabling a single readout plane to instrument a larger drift length (vital for obtaining the large fiducial volume required for WIMP detection in a gas). Certain negative ion drift gasses or mixtures also have minority charge carriers, which enables the drift distance (i.e. its z coordinate) of an ionisation event to be determined due to the different relative drift speeds of the charge carriers, which is advantageous for vetoing noise events originating from the anode or cathode. One of the challenges of operating a TPC with a negative ion gas however, is that electrons need to be stripped from the negative ions before an avalanche can be initiated; meaning much higher electric fields are required than in electron drift gasses to achieve comparable gas gains. In DRIFT for example, the MWPCs typically achieved avalanche gains of less than 10^3 [8].

The CYGNUS consortium, a new world-wide grouping of directional DM efforts, has sought to address these issues through new readout concepts, such as pixels and Micromegas, combined with gain stages such as Thick Gas Electron Multipliers (ThGEMs) [9]. These concepts seek to achieve higher spatial resolution (< 200 µm) and gas gain (dependant on readout type, but generally $> 10^3$), and hence lower energy thresholds and better sensitivity to low mass (sub-10 GeV) WIMPs. NITPCs with SF_6 have also been developed for its improved handling over CS_2 and large fluorine fraction, critical for spin-dependent WIMP sensitivity. Like CS_2 (mixed with O_2) SF_6 also produces minority carriers that aids background control by allowing determination of the absolute position of events [10].

The MM-ThGEM work discussed in this paper forms part of this program. In this paper the design and operating principles of the MM-ThGEM are presented. Following this, the biasing setup for the MM-ThGEM and the methods for measuring the gas gain in CF_4 and SF_6 with a ^{55}Fe source are discussed. Subsequent sections focus on the different regions of the device specifically looking at the effect of field strength on gain. Starting with the collection field, pure CF_4 and pure SF_6 are used alongside supplementary Garfield++ simulations to investigate the collection efficiency. Pure CF_4 is not used in the in later measurements because it does not require a second amplification

2023 JINST 18 P08021

stage. The effect of varying the amplification fields is then investigated in pure SF_6 and Townsend parameters are extracted. Then the strength of the transfer fields are subject to testing and an ion feedback phenomenon is reported. Finally, some gain measurements with the device in CF_4:SF_6 mixtures are presented. This was included because such mixtures have been found to retain the characteristics of pure NI gas, including production of minority carriers, yet have the advantage of greatly reducing the amount of SF_6 needed [11]. This mitigates against the potential environmental effects of SF_6, which is a more potent greenhouse gas than CF_4.

As indicated, the MM-ThGEM is intended here to provide only a charge amplification stage for a full readout plane such as xy-strip or micromegas. Practically, these would best be integrated into one PCB package to minimise charge losses or diffusion between MM-ThGEM and readout. However, for simplicity in this work and to minimise risk of damage from discharges, the MM-ThGEM used here was a stand alone device. Operation in conjunction with an example Micromegas plane will be covered elsewhere.

2 MM-ThGEM design and operating principles

MM-ThGEM used in this work, shown in figure 1 and described below, was designed and fabricated in collaboration with the CERN Micro-Pattern Gas Detector (MPGD) group. The device is to act as a charge avalanche plane for coupling to a Micromegas or similar readout to yield high gain with NI gases and mixtures, notably with SF_6. It builds on the standard ThGEM that consists of a dielectric sheet with typically sub-millimeter thickness coated on both sides by a thin copper layer [12]. In conventional hole type multipliers, such as ThGEMs, holes are drilled through the sheet such that when a voltage is applied between the copper layers a strong dipole field is formed. ThGEMs have proved highly successful at producing electron amplification in electron drift gases [13, 14]. However, with the NI gas SF_6, the nature of the gas and the high fields needed to strip off the attached electrons are found to cause instabilities and potentially damaging sparks that limit the achievable gain.

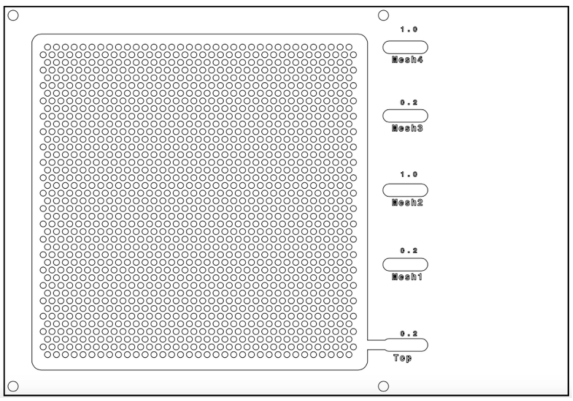

(a) Plan diagram of the MM-ThGEM.

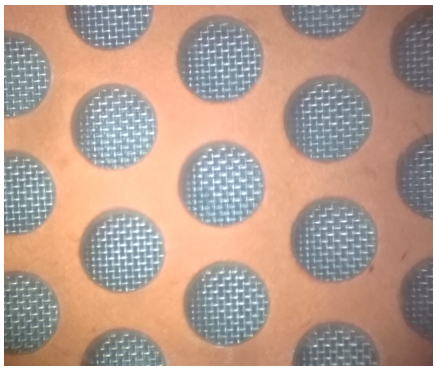

(b) Close-up picture of the MM-ThGEM holes from above.

Figure 1. A plan view of the MM-ThGEM detector and a close-up of the holes.

Figure 2 shows a cross section schematic of the design of the MM-ThGEM used in this work. The MM-ThGEM has the same form as a ThGEM, with dielectric copper planes top and bottom

2023 JINST 18 P08021

and a lattice of holes. However, a set of four mesh planes is added, layered into the dielectric sheet and across the holes. These planes provide added control over the field shape within the holes and are expected to help mitigate some of the issues experienced with standard ThGEMs in NI gasses. In particular sparking across the dielectric surface which is believed to be a significant source of the damage that has been observed by us to degrade ThGEM performance.

Referring again to figure 2, it can be seen that the meshes and copper planes of the MM-ThGEM divide the detector into six distinct field regions. These are termed the drift field, collection field, first amplification field, first transfer field, second amplification field and second transfer field. The top of the drift region is delimited by the cathode (not shown), and is the volume in which ionising interactions in the drift gas generate the primary electrons which are then collected by the device for amplification. The device has an amplify-drift-amplify configuration where collected charge from an event is amplified in one high field region then drifted in a low field region before being amplified again in the second high field region. For convenience the meshes are labelled 1 to 4 from top (cathode side) to bottom and the copper planes referred to as the top and bottom planes. The meshes are a square weave steel mesh with ≈20 µm wire diameter and ≈60 µm pitch. The amplification regions are generated between meshes 1 & 2 and meshes 3 & 4. The gaps between the mesh pairs is 200 µm, their positions being 200 µm, 400 µm, 1400 µm and 1600 µm respectively from the top, the total device thickness being 2600 µm. The other field regions (drift, collection and transfer fields) are used for charge transport. Each region is delimited by a mesh except for the collection and drift fields which do not have a specific boundary and are more interdependent than the other fields. The holes have diameter 0.8mm with hexagonal lattice pattern of pitch of 1.2mm over the 10 x 10 cm active area.

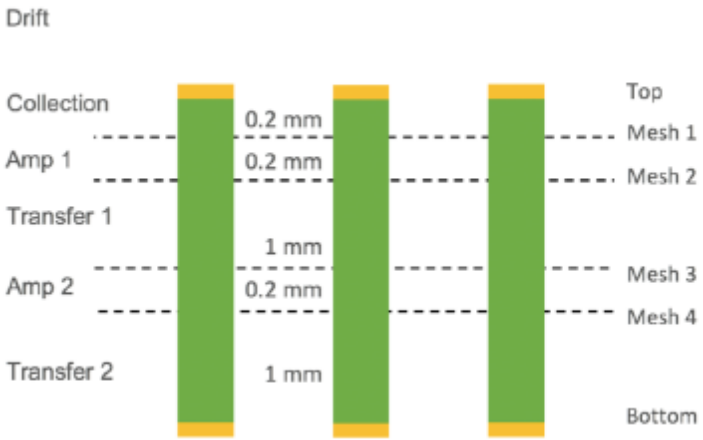

Figure 2. Schematic of the MM-ThGEM used in this work.

3 MM-ThGEM set-up and calibration

For the tests here the MM-ThGEM was operated inside a purpose-built steel vacuum vessel, as shown in figure 3. The drift volume of the MM-ThGEM detector was formed by a square copper plate cathode which was positioned 13 mm above the top plane of the MM-ThGEM using nylon rods. An ^{241}Am α and ^{55}Fe x-ray source were sealed in the vacuum vessel with the detector and

2023 JINST 18 P08021

manipulated into position with magnets. The biasing scheme used is shown in figure 4. Meshes 2 and 4 were biased and instrumented through a CR-150 Cremat charge sensitive preamplifier board [15] which has an internal low-pass filter and can mount one of a number of charge sensitive preamplifiers. For meshes 1 and 3 external filters were implemented, necessary because the small separation and relatively large mesh areas results in a significant capacitive coupling between adjacent meshes and hence noise if no filters are implemented. The MM-ThGEM top plane was grounded through a 100 MΩ resistor, the bottom plane was left floating. The amplification chain for the instrumented meshes (2 and 4) comprised a Cremat CR-111 preamplifier and CR-200 4 µs shaper, the latter located outside the vessel, the former mounted on the CR-150 boards and located inside the vessel to help minimise noise. Digitisation was via a National Instruments NI-5751 unit, self-triggered with a software threshold and digitisation window of ±1000 µs from the trigger time, the signal sampled every 1 µs.

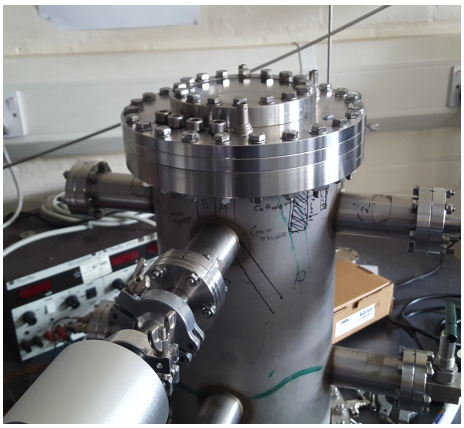

Figure 3. Picture of the vessel with the MM-ThGEM setup inside.

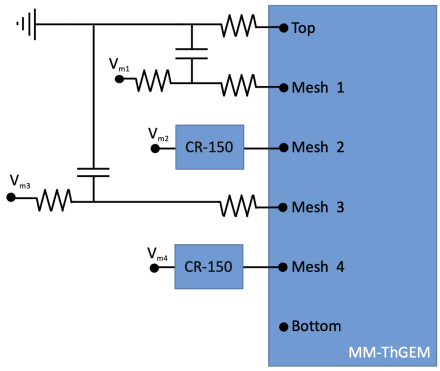

Figure 4. Circuit diagram of the bias scheme of the MM-ThGEM.

To determine total gains in the MM-ThGEM tests, the electronic gain from the amplification chain needs to be determined. The conventional means was adopted for this of injecting a test pulse through the 15 pF capacitor on the CR-150 board. Two parameters were extracted for this to account for two metrics adopted for measurement of the final signal; the maximum voltage of the signal peak and the integrated peak voltage. The former is suitable when the charge collection time is faster than the shaping time of the electronics (usually 4 µs here) for instance for electron drift gasses like CF_4. When the collection time is slower than the shaping time not all the collected charge contributes to the measured peak height, thus integrating the peak signal provides a better gain measurement for NI drift gases such as SF_6. Calibration with the test pulse demonstrated that both metrics are linear with injected charge for the amplification setup adopted. The electronic gain values for the amplification chain (preamplifier and shaper) obtained were respectively 0.402 ± 0.003 V pC^{-1} for the peak voltage form and 7.46 ± 0.06 V µs pC^{-1} for the integral.

4 MM-ThGEM collection field in CF_4

In conventional ThGEMs the collection field that directs the charge into the holes is part of the same field responsible for the amplification. In the MM-ThGEM the mesh layers provide separation of

2023 JINST 18 P08021

fields so that it is possible for collection and amplification processes to occur in separate fields and therefore to be controlled independently. The collection field is generated by the voltage between the cathode, MM-ThGEM top plane and first mesh; as such its shape is affected by the drift field which has no hard boundary (such as a mesh layer) dividing it from the collection field. Efficient focusing of the charge into the holes is vital, so a detailed study of the behaviour of the field arrangement is important, specifically how the voltage between first mesh and top plane shapes the collection field and affects the focusing of charge into the holes, and hence the gain and energy resolution. Operation with CF_4 is suited to this study because it has significantly higher gas gain than SF_6 and, as an electron drift gas, is more straightforward to model. The following outlines first experimental work on this together with results from a charge transportation model.

4.1 Experimental measurement of gain and energy resolution

The CF_4 tests were conducted at 40 Torr using the setup described in section 2 and 3. The ^{55}Fe x-ray source (producing 5.89 keV x-rays) was moved close to the detector drift volume to produce low energy electron recoils. The ionisation energy (W) of CF_4 is 34 eV [16] so an average of 173 primary electrons are produced by the 5.89 keV ^{55}Fe x-rays. It was found that sufficient gain could be reached to observe ^{55}Fe events even with only one of the two amplification fields active; requiring only one amplification field to observe ^{55}Fe enabled the collection field to be studied with fewer systematic effects arising from processes occurring in subsequent transport through the device. Meshes 3 and 4 were therefore left grounded and a constant potential difference of 530 V was maintained between meshes 1 and 2, equating to an amplification field of 26 500 V cm^{-1} which is sufficient to produce a clear ^{55}Fe spectral peak. The cathode voltage, V_{cath}, and mesh 1 voltage, V_{m1}, were then varied from −100 V to −500 V and 10 V to 170 V respectively. The output of the amplification chain of mesh 2 was connected to an Ortec 926 ADCAM Multichannel Buffer (MCB) [17]. Figure 5 shows an example ^{55}Fe spectrum at $V_{m1} = 30$ V and $V_{\text{cath}} = -200$ V demonstrating the expected spectral peak superimposed on ambient background and rising noise at low energy.

A Gaussian was fitted to each 5.9 keV peak together with an exponential to account for the background; the fitted function is shown as a red line in figure 5. The mean and width of the Gaussian was used to determine the gain and energy resolution, the former calculated via the calibration in section 3 and the W-value of the gas and the latter given by the FWHM divided by the mean. Figure 6 shows results for this vs. cathode and mesh 1 voltages.

Figure 6 shows the gain and energy resolution for different cathode voltages against mesh 1 voltage (as the top plane is grounded the mesh 1 voltage is equal to the potential difference between the top plane and mesh 1). Two particular regimes are found: for $V_{m1} \lesssim 60$ V the gain is inversely related to the cathode voltage and close to flat with V_{m1}, conversely when $V_{m1} \gtrsim 100$ V the gain exponentially increases with V_{m1} and proportional to the cathode voltage. There is significant spread in the energy resolutions found for the different cathode voltages at low collection fields, with higher cathode voltage having worse energy resolution. At higher collection fields the energy resolution becomes more similar for each value of the cathode voltage.

2023 JINST 18 P08021

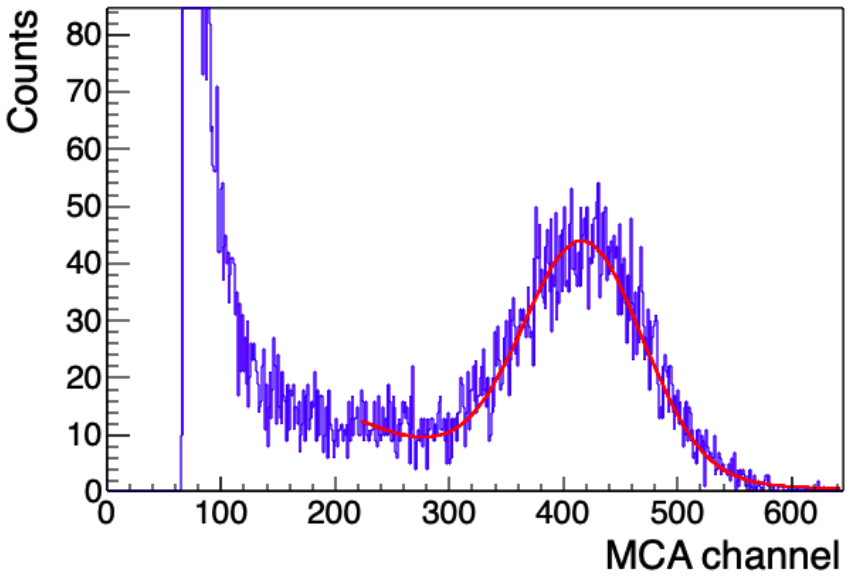

Figure 5. MM-ThGEM mesh 2 MCA spectrum (blue) and fitted peak (red) from an ^{55}Fe run in 40 Torr CF_4 with $V_{m1} = 30$ V, $V_{\text{cath}} = -200$ V and an amplification field of 26 500 V cm^{-1}.

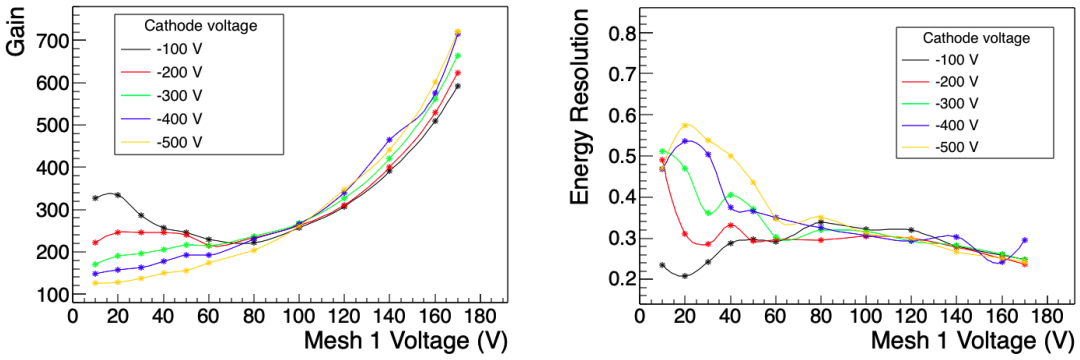

Figure 6. Gain Vs Mesh 1 voltage (left) and energy resolution (right) of the MM-ThGEM for different cathode voltages in 40 Torr CF_4 with a single amplification field operating at 26 500 V cm^{-1}.

4.2 CF_4 charge transport simulation in Garfield++

The non-linearity of the gain and energy resolution with the drift and collection fields found above suggests that competing processes are likely occurring. To better study the contributions of these to the signal a Garfield++ simulation of the charge transport in the MM-ThGEM was developed, focused on the region between the cathode and mesh 1 to understand the processes of transport and multiplication in the drift and collection fields. An electric field map was first generated for each set of cathode and anode voltages using the ANSYS finite element code, cross sections of the MM-ThGEM top between adjacent holes with example voltages from this are shown in figure 7. The volume of the field map was defined by the cathode and mesh 1 planes and a rectangle with opposite corners at the centre of adjacent holes (corresponding to the rectangle in figure 8, described

2023 JINST 18 P08021

below). The map for the MM-ThGEM's hexagonal lattice of holes was created by reflection along each edge of the rectangle.

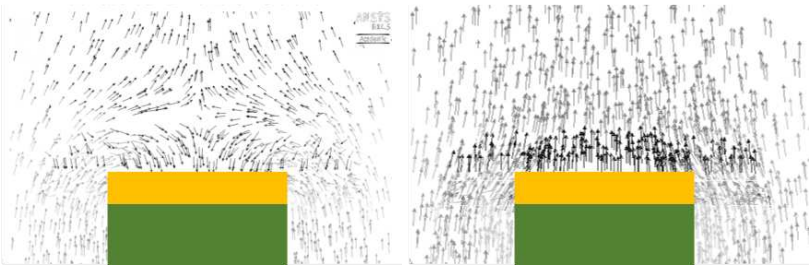

(a) V_{m1} = 20 V, V_{cath} = 100 V. (b) V_{m1} = 20 V, V_{cath} = 500 V.

Figure 7. Sample MM-ThGEM ANSYS maps of the collection field for different cathode voltages with mesh voltage V_{m1} = 20 V.

Referring to figure 7, the direction of the arrows in the field maps indicates the direction of the electric field and the length of the arrows indicates the field strength. The left and right edges of each map correspond to the centres of adjacent holes and the dielectric and metal between the holes is indicated in green and orange. The maps vary from having a dipole-like shape where the electric field exiting the hole loops back to be directed toward the metal as in figure 7a, to the field being close to linearly orientated in the cathode direction as in figure 7b. The field shape is dependent on the ratio between the cathode and mesh 1 voltage, with larger V_{cath}/V_{m1} producing more linear field shapes and smaller V_{cath}/V_{m1} producing more dipole-like field shapes

The field maps were imported to Garfield++ and 10000 electrons randomly placed within the boundaries of the field map rectangle cell 8 mm above the MM-ThGEM top plane. Garfield was then used to transport each electron in 40 Torr CF_4 in the electric field and the endpoints recorded. The position and status flag of each endpoint was used to determine if the electron had been successfully collected by reaching the first mesh or if it had attached in the gas or ended up in the dielectric or top plane of copper. Figure 8 shows an example spatial distribution of endpoints with V_{m1} = 60 V and V_{cath} = 300 V. Here the electrons embedded in the dielectric walls of the holes, shown by blue markers, outline the edges of the MM-THGEM holes near the electrons' starting location. The collected electrons, in green, are located at the bottoms of holes on the plane corresponding to mesh 1. Finally electrons which attach in the gas, in cyan, are broadly found in the hole centres. Electrons impacting on the copper top plane of the MM-ThGEM were not present at all at this voltage.

In addition to electron losses, electrons are also generated in an avalanche process at some voltages. Figure 9 shows the rates of electron generation and losses found with different field configurations. Figure 9a shows the simulated gas gain for the collection field, determined by the total electron endpoints divided by the starting number of electrons. At mesh 1 voltages of 20 V and 40 V no electron multiplication is observed in the collection field. Above 60 V the gain rises exponentially. There is also a slight proportionality to cathode voltage. This can be attributed to the drift field contributing slightly to the field in the hole. Figure 9b shows the fraction of endpoints which were located on the top copper plane, collected by the device, embedded in the dielectric and attached to ions in the gas. These four scenarios account for all of the electron endpoints in the simulation. At low V_{m1} and high V_{cath} most of the electron losses are to the top copper plane,

2023 JINST 18 P08021

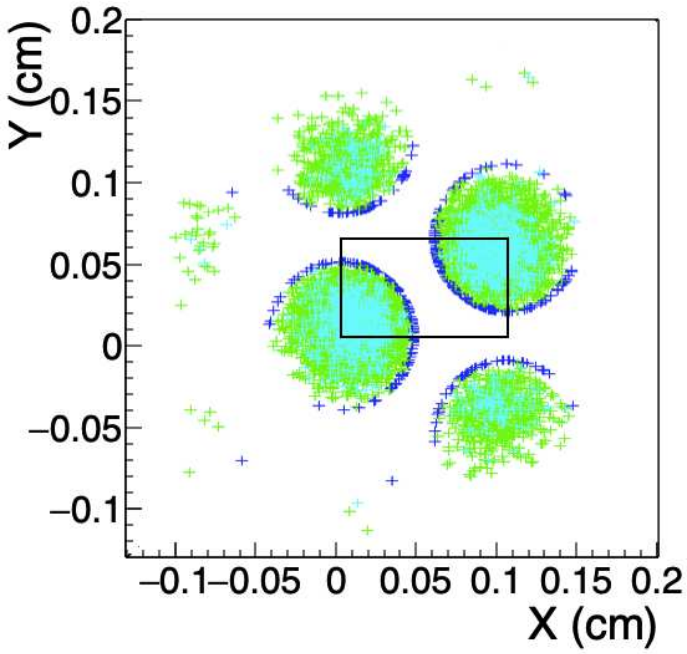

Figure 8. Electron endpoint distribution in space for V_{m1} = 60 V, V_{cath} = 300 V. Cyan: attached, Green: collected, Blue: embedded in dielectric.

this can be explained by the geometry of the electric field; at low values of $\frac{V_{m1}}{V_{cath}}$ the field above the top plane is close to uniform and the electrons will move close to straight down from their starting positions with many ending up on the metal. When $\frac{V_{m1}}{V_{cath}}$ is higher the field above the hole takes on a more dipole shape and better directs the electrons into the holes reducing the fraction of electrons lost in this way to zero. The difference in field shapes is demonstrated by figure 7a and figure 7b.

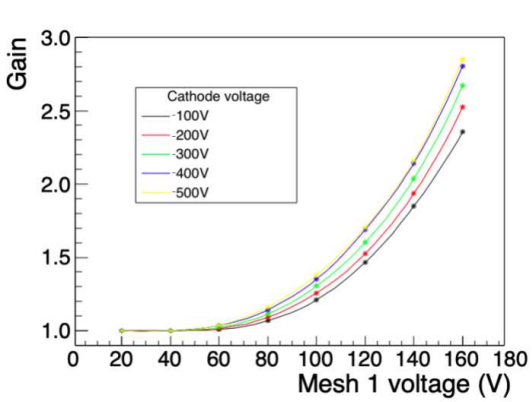

(a) Gas gain vs mesh 1 voltage.

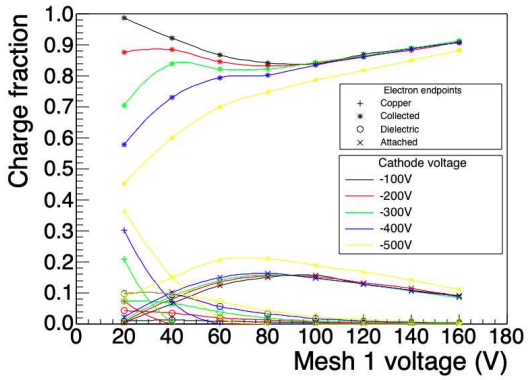

(b) The ratios of the electron endpoint locations against mesh 1 voltage.

Figure 9. Results for Garfield++ simulation of electron transport in the collection and drift fields of the MM-ThGEM in CF_4 for different cathode voltages.

2023 JINST 18 P08021

Electron attachment in the gas dominates the losses for high V_{m1}, with minimal dependence on the cathode voltage, except for $V_{\text{cath}} = -500\,\text{V}$ which shows enhanced attachment. In CF_4 the electron attachment coefficient increases at high E/N starting at around $35\times10^{-17}\text{Vcm}^2$ [18], equivalent to around $495\,\text{V}\,\text{cm}^{-1}$ or a cathode voltage of $-380\,\text{V}$. The high fields generated in the holes are enough to cause significant electron attachment which increases with the collection field until the effect starts to be offset by the gas gain. In the case of $V_{\text{cath}} = -500\,\text{V}$ the drift field is enough to cause significant attachment in the drift region causing additional losses as compared to lower cathode voltages. The dependence on field is reflected by the distribution of electron attachment endpoints in figure 8, which are concentrated in the holes of the MM-ThGEM.

The last component of electron losses in figure 9b is electrons embedding in the dielectric sides of the holes. The rate of losses here decreases with increasing V_{m1} and shows an approximately linear relationship with cathode voltage. There are no hole rims in this MM-ThGEM design so to embed in the dielectric the charge needs to diffuse laterally within the hole. The lower proportion of electrons terminating in the dielectric at high V_{m1} and low V_{cath} is a result of better focusing of the electrons into the centre of the hole. Electrons embedding in the dielectric would tend to cause charging there, resulting in focusing of charge in the hole, although back flowing positive ions will counteract this which could result in a net positive charge on this part of the hole wall [19]. Currently the general effect of charge up has not been studied. It might contribute to the shape of the collection field over long exposure times though this is not an issue for DM experiments because event rates are low.

To compare the simulation to the data one can define the effective gain of the drift and collection fields of the MM-ThGEM as the number of electrons which arrive at the first mesh divided by the initial number of electrons. Figure 10 shows the effective gain determined in Garfield, it preserves a number of the trends of the experimental data which is shown in figure 6. The large difference between absolute gain values in the modelled and experimental data can be attributed to the lack of any consideration in the modelled data of transport through and after mesh 1; neither mesh transparency nor gain in the first amplification field are considered.

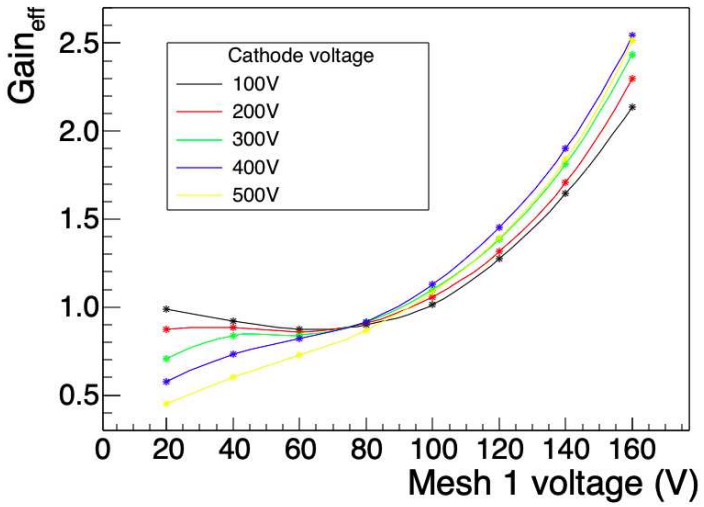

Figure 10. The simulated effective gain of the MM-ThGEM drift and collection fields.

2023 JINST 18 P08021

The exponential nature of the gain with mesh 1 voltage is a common feature of the simulated and experimental data, as is the proportionality of the gain with cathode voltage at high V_{m1} and the inversion of that proportionality at lower mesh 1 voltage. The most significant difference is in the region $V_{m1} < 60\,\mathrm{V}$, particularly for $V_{\mathrm{cath}} = 100\,\mathrm{V}$ which in the data has a gain approximately 1.5 times higher for $V_{m1} = 20$ than for $V_{m1} = 80$ compared to 1.1 times higher in the simulation. This difference might be attributed to better transport of the electrons through mesh 1 at lower collection fields in the experiment, a process not simulated in Garfield.

Regarding the influence of collection field on the energy resolution, the main effect will be due to variation in the number of electrons collected at mesh 1. The simulation doesn't model the energy resolution of the device but it is likely that the main contributor from the collection field is electrons lost to the metal and dielectric. This is seen to decrease as V_{m1} is increased, compatible with the general improvement in energy resolution seen in the data. Also the localised nature of the electron recoils that the system detects means that the alignment of an initial charge cloud with a hole would have a significant effect on the efficiency of the charge collection at low collection fields. The attachment rate on the other hand is not really dependent on the initial position and hence would contribute more to a lowering of the gain than degradation of the energy resolution. This is reflected in the experimental data by the generally larger energy resolution at low V_{m1}.

4.3 Conclusions

In summary the CF_4 experiments confirmed how the collection field is an important factor contributing to the gain and resolution of the MM-ThGEM. Most reliable operation was found above $V_{m1} \gtrsim 100\,\mathrm{V}$ a region where both gain and energy resolution improve as V_{m1} is increased, with little dependence on cathode voltage. With some slight differences the simulated Garfield++ data reflects well the variation in the gain observed experimentally and assisted in determining how electron multiplication, attachment, and impact on the metal and dielectric contribute to the final gain. The change seen in the proportions of charge lost in the metal and dielectric are likely compatible with changes in the energy resolution with mesh voltage observed experimentally.

5 MM-ThGEM collection field in SF_6

Having explored the operation of the MM-ThGEM collection field in the electron transport gas CF_4, attention shifts here to use with the SF_6 negative ion (NI) drift gas. As outlined in section 1 NI gases are useful mostly because of the reduction in diffusion of the drifted charge clouds. However, the device performance is expected to be considerably different as the charge carriers are ions not electrons. As discussed in section 4, ensuring efficient collection of the charge by the collection field, which functions to channel charge into the MM-ThGEM holes, is key. However, in a NI gas the efficiency of the field at focusing charge into the holes is expected to be the only way that the collection field influences the gain as there is not expected to be any significant gas gain or reattachment occurring as seen in CF_4.

5.1 Experimental measurement of gain and energy resolution

In pure SF_6 it was early on found that both amplification fields were required to get a clear ^{55}Fe spectral peak. So for these tests signals were taken from the last mesh plane (mesh 4 in figure 2).

2023 JINST 18 P08021

The detector was operated at 20, 30, 40 and 50 Torr. Once a stable operating point was found the collection field was varied with the other fields held constant. Table 1 shows the electric fields and pressure operating points used and figure 11 shows results for the total gain vs. mesh 1 voltage for each pressure, the gain determined here from the integral of the signal waveforms (see section 3). The ionisation energy of SF_6 is 34 eV (the same as CF_4) and so 173 primary electrons are produced by the ^{55}Fe x-ray [20].

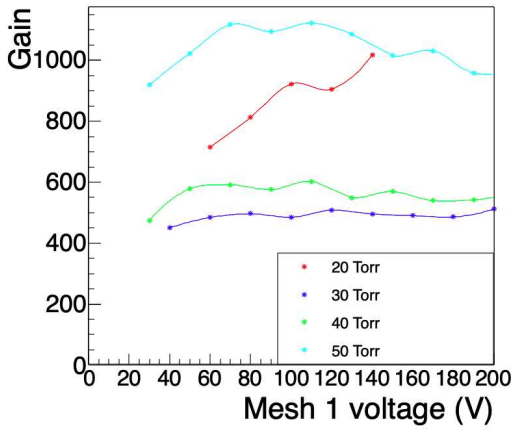

Figure 11. Measured gas gain for different pressures of SF_6 vs mesh 1 voltage.

Pressure (Torr)	Transfer ($V\,cm^{-1}$)	Amp 1 ($V\,cm^{-1}$)	Amp 2 ($V\,cm^{-1}$)	Cathode (V)
20	400	22000	21000	500
30	600	23500	23500	500
40	600	25000	25500	600
50	600	28500	24500	600

Table 1. Bias settings at each pressure when changing the collection field.

As seen from table 1 the amplification fields required to observe ^{55}Fe were found to increase with pressure. This is expected as the mean free path of the stripped electrons being amplified gets shorter as the pressure increases, which necessitates higher fields to produce the same gains. The effect of changing the amplification fields on gain and energy resolution is covered further in section 6. As shown in figure 11, there is found to be little variation in the gain as the collection field increases, except at 20 Torr where a general increase is seen. This and other irregularities seen at 20 Torr are discussed further in section 8. Overall the near flat gain response with mesh voltage suggests charge is collected with optimal efficiency above 30 V to 40 V, rising to between 60 and 80 V at 40 and 50 Torr for the cathode voltages and pressures explored.

5.2 SF_6 charge transport simulation in Garfield++

As with the CF_4 work of section 4, the influence of collection field on observed gain in SF_6 can be explored using Garfield++. However, this code does not support transport and amplification of negative ions so instead positive ion transport was used, reversing the electric fields and setting the ion mobility manually to that of SF_6^-. A consequence is that deattachment and amplification processes are not simulated. However, these are expected to be negligible in SF_6 at the collection fields of interest. On this basis, and using the same methodology of section 4, figure 12 shows example results for the collection efficiency into the holes vs. mesh 1 voltage V_{m1} for 40 Torr SF_6.

The results show that for a given cathode voltage the fraction of charge collected increases with V_{m1}, reaching close to 100% at $V_{m1} > 60$ V for all of the cathode voltages used. This flat relationship for $V_{m1} > 60$ V is consistent with the experimental data at pressures above 20 Torr (see figure 11). However, we now see that the actual V_{m1} required to achieve the maximum increases

2023 JINST 18 P08021

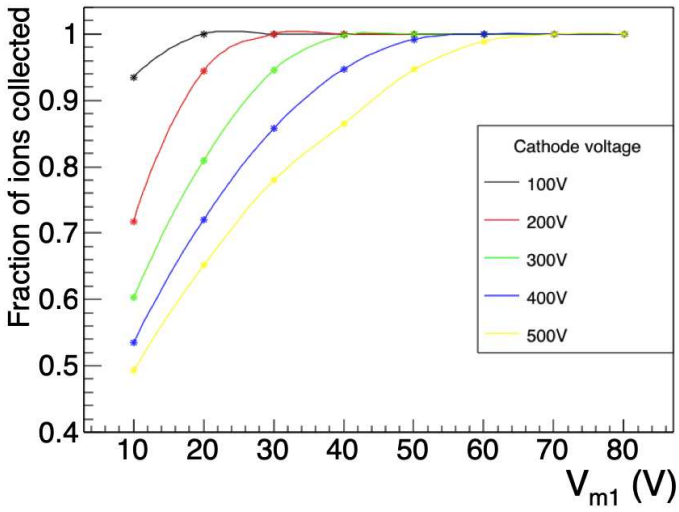

Figure 12. Simulated collection efficiency of MM-ThGEM drift/collection fields in 40 Torr SF_6.

with cathode voltage, consistent with the field shape rather than strength being the main factor determining collection efficiency. For each of the cathode voltages explored total charge collection is achieved at a collection to drift field ratio of around 10:1. All the uncollected ions were found to end up on the metal top plane, different from the CF_4 electron case where a significant fraction of charge not collected or reattached ended in the dielectric. This is likely attributed to the lower diffusion rate for the ions compared to electrons; once the charge has entered the hole it must diffuse laterally to reach the dielectric and embed, this happens at a lower rate for ions than electrons. The lack of attachment, electron multiplication and charge embedding in the dielectric means the amount of charge reaching the first mesh is equal to the amount channeled into the holes.

5.3 Conclusions

In summary, the results show that switching from CF_4 electron drift to SF_6 negative ion drift significantly changes the charge transport in the collection field as expected. Both simulation and the experimental data suggest that a potential difference of order 70 V between mesh 1 and the top copper plane is sufficient to achieve near total charge collection for drift fields $\lesssim 400\,\mathrm{V\,cm^{-1}}$. No significant benefit in total effective gain or energy resolution is seen for higher collection fields or higher drift fields.

6 MM-ThGEM amplification fields in SF_6

Having determined the optimum collection field for efficient transport of charge into the holes using SF_6 (see section 5), focus moves here to study and optimisation of the two amplification regions responsible for multiplication of the charge and key to determining the overall gain. The two regions (see figure 2) are defined by meshes 1 and 2 (amplification field 1) and meshes 3 and 4 (amplification field 2). Charge is transported between these by a transfer region with weaker field. As noted in section 5, the gain from a single amplification field was found not to be sufficient to observe a clear ^{55}Fe peak with SF_6, so all measurements here had both amplification fields in operation. Disentangling the contributions to the gain from each thus required some novel approaches.

2023 JINST 18 P08021

6.1 MM-ThGEM gain with equal amplification fields

The first approach used was to set the amplification fields equal. This has the advantage that the gain of each stage should be equal. It also reduces the number of bias parameters to be optimised. For these runs V_{m1} was set to 30 V, the cathode voltage 500 V and the transfer field 500 V cm^{-1} at 20 Torr and 600 V cm^{-1} at 30 and 40 Torr. The amplification fields were kept identical at all times. Figure 13 shows results for the total gain, using the ^{55}Fe 5.9 keV peak from the integrated mesh 4 signal, vs. amplification fields at 20, 30 and 40 Torr SF_6. The lowest field setting at each pressure was determined by the gain required to distinguish a clear ^{55}Fe peak. Readings at higher gains for 20 and 30 Torr were limited by the onset of breakdown noise (discussed further in section 8), and to limit potential damage at 40 Torr the amplification field was kept below 25 000 V cm^{-1}. As shown in figure 13 the trend is for an exponential increase in gain with amplification field. At 20 Torr, a gain measurement could only be made over a narrow window of operating voltages from 21 000 V cm^{-1} to 22 000 V cm^{-1}, whereas at 30 Torr the 5.9 keV peak was observable over almost twice this, from 21 500 V cm^{-1} to 24 500 V cm^{-1}. The highest gas gain, approximately 3000 was observed at 30 Torr.

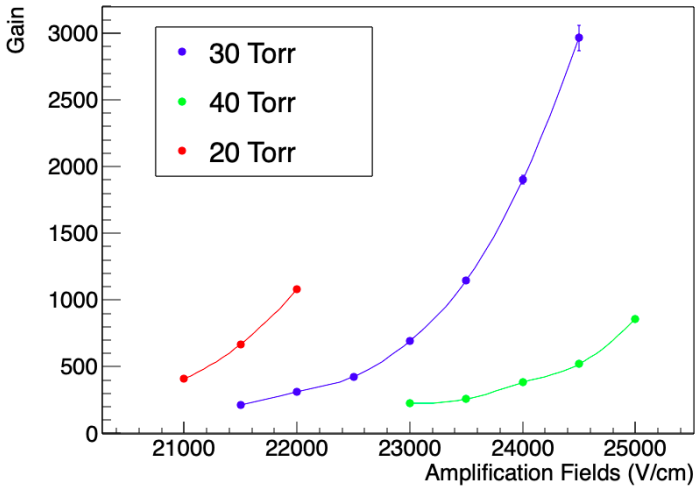

Figure 13. MM-ThGEM total gain at 20, 30 and 40 Torr SF_6 against amplification field when amplification fields 1 and 2 are equal.

6.2 MM-ThGEM gain dependence on amplification field 2

Finally, the influence on energy resolution and total MM-ThGEM gain of the second amplification field was explored using ^{55}Fe, again with all other fields fixed at nominal values for each pressure but now with the gain determined from 5.9 keV ionisation peak. The transfer field was set to 600 V cm^{-1} in all runs. V_{cath} and V_{m1} were set to 500 V and 140 V respectively for the 20 and 30 Torr runs and 600 V and 150 V for the 40 and 50 Torr runs. The first amplification field was set to 22 000 V cm^{-1}, 23 500 V cm^{-1}, 26 000 V cm^{-1} and 28 500 V cm^{-1} respectively for the 20, 30, 40 and 50 Torr runs.

Figure 14 shows the resulting gain and energy resolution data against the second amplification field for each pressure. From figure 14a we see that the total MM-ThGEM gains at the fields chosen were of order 100, suggesting gains of order 10 per individual amplification region (including losses due to mesh transparency, etc.). The gain rises with amplification field as expected though with

2023 JINST 18 P08021

slightly different forms depending on the pressure. At 50 Torr and in the higher field regions of the 30 and 40 Torr, the relationship appears linear. At 20 Torr and at the low field regions of the 20 and 30 Torr data there is an upward curve suggestive of a exponential relationship. Figure 14b shows the dependence of energy resolution (FWHM over mean of the gaussian fitted to the 5.9 keV peak) on amplification field 2. Overall the energy resolution is worse than was seen in CF_4 as expected due to the necessity in SF_6 to strip electrons from the negative ions. For the 30, 40 and 50 Torr data, a minima in energy resolution is seen, whereas for 20 Torr data the resolution steadily degrades with increasing field. This is possibly attributable to the feedback effect discussed later in section 8. The lowest obtained energy resolution is seen to decrease with increasing pressure, the lowest being about 60% in 50 Torr.

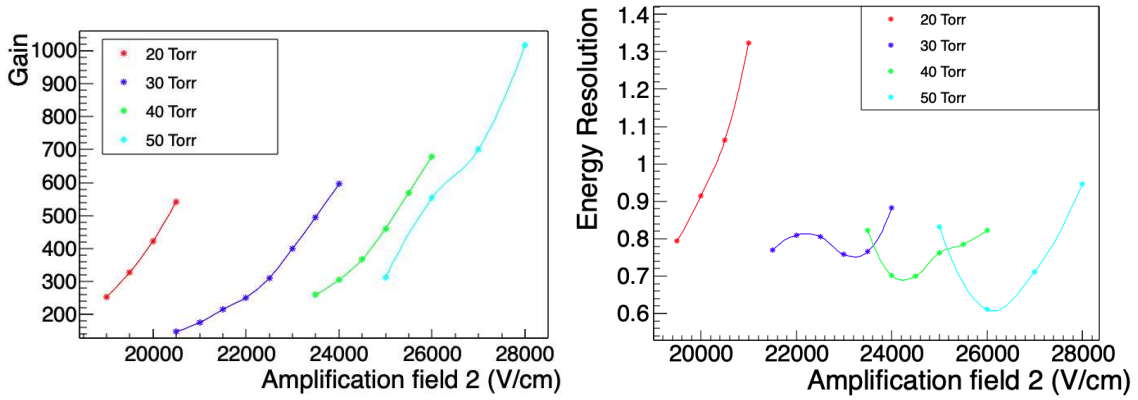

(a) The effective gain vs amplification field 2.

(b) The energy resolution vs amplification field 2.

Figure 14. Plots from variation of second amplification field of MM-ThGEM in low pressure SF_6 when first amplification field is held constant.

Significantly the lowest energy resolution at each pressure is not obtained when the amplification fields are equal but instead when the second amplification field is smaller than the first. The energy resolution minima also appear correlated to the approach of the break in gain response seen. The paper [21] suggests that such minima might result from a trade-off between the increased resolution of a larger amount of charge reaching the detection element and degradation in amplification associated with approaching the maximum operating voltage. In any case determining the locations of these minima will be important to fixing optimal operating points for the device.

6.3 Extracting Townsend gas parameters

For completeness it is useful now to compare the gain of the device with the well known Townsend equation, an analytical model for gas gain in a linear electric field. The first order Townsend equation for a one stage device can be given as:

$$\ln(Gain) = dPAe^{-\frac{BP}{E}} \tag{6.1}$$

where d is the width of the amplification gap, P is the pressure, E is the amplification field, and A & B are the Townsend coefficients associated with the gas in which the amplification is occurring.

2023 JINST 18 P08021

For a two stage device the total gain will be a multiple of the two gains:

$$\ln(Gain) = \ln(G_1 G_2) = \ln(G_1) + \ln(G_2) = d_1 P A e^{-\frac{BP}{E_1}} + d_2 P A e^{-\frac{BP}{E_2}} \tag{6.2}$$

this can be reformulated as a linear equation if $d_1 = d_2$ and $E_1 = E_2$ in the form of

$$\ln(\ln(Gain)) = \ln(2dPA) - \frac{BP}{E}. \tag{6.3}$$

assuming perfect collection and transfer of charge. This can also be reformulated to give the mean free path of electrons, λ, and effective ionisation coefficient, I_e using the Rose-Korff formulation.

For a detector well characterised by the Townsend equation, the double natural logarithm of the gain is expected to be linear with the inverse amplification field. As shown in figure 15 this is indeed found for the data here with gains determined when the amplification fields are equal.

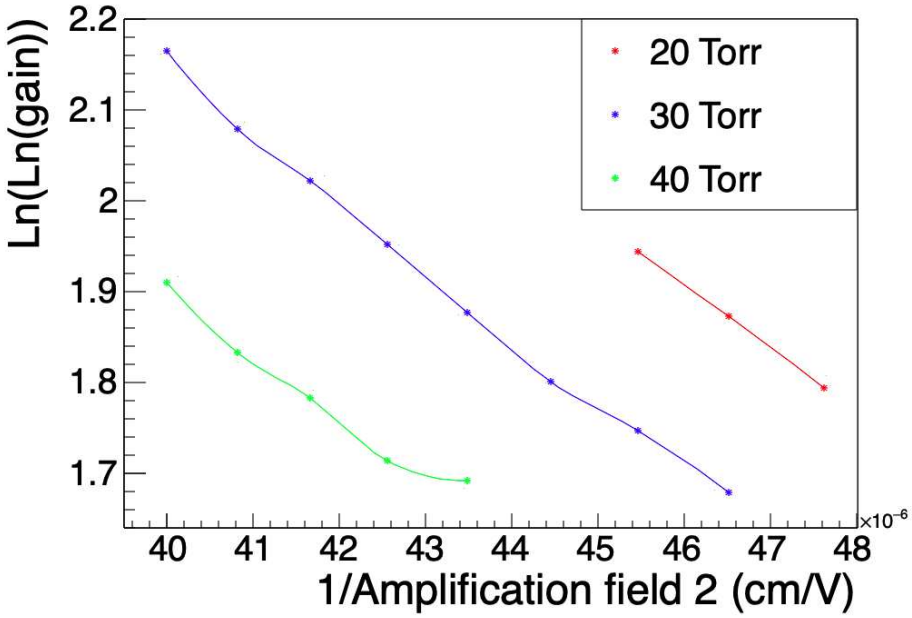

Figure 15. The double log of the effective gain of the MM-ThGEM in SF_6 against inverse amplification field where amplification field 1 equals amplification field 2.

Based on this a linear fit to the points on figure 15 can be used to obtain the values A, B, λ and I_e for each pressure. The results are shown in table 2.

Table 2. Townsend coefficients, mean free path and ionisation energy from the MM-ThGEM.

Pressure (Torr)	**A (cm^{-1} $Torr^{-1}$)**	**B (V cm^{-1} $Torr^{-1}$)**	λ **(μm)**	I_e **(eV)**
20	201 ± 10	3500 ± 50	2.49 ± 0.12	17.4 ± 0.9
30	176.5 ± 15	2666 ± 66	1.89 ± 0.16	15.1 ± 1.3
40	89.0 ± 30	1909 ± 120	2.81 ± 0.95	21.4 ± 7.4

Considering table 2 note first the trend for A and B to decrease with increasing pressure. This is as expected, consistent with the effect observed in the negative ion gas CS_2 for instance [22]. The

2023 JINST 18 P08021

effective ionisation energy, I_e, should be constant with pressure therefore it is reasonable to obtain a weighted average from the values at different pressures. This yields an I_e of 16.7(5) eV. I_e is not expected to match the ionisation energy exactly because some of the energy obtained by the electrons accelerated in the amplification field is dissipated by prior collisions. Nevertheless, the value is close to typical previous measurements, for instance 15.32(2) eV by [23]. The estimated free path length, λ, should be inversely proportional to pressure. This is not observed in the values extracted. However, one factor neglected from this analysis is losses during charge collection and in transfer between the amplification regions due to, for example, mesh transparency. These would contribute additional terms to equation (6.3). The inclusion of terms to account for charge losses was considered, however the resultant mixing of linear and exponential terms produced large errors in any results.

6.4 Conclusions

In summary, though further optimisation of the MM-ThGEM is still required for SF_6 operation it is clear that gains sufficient to observe 5.9 keV electrons from ^{55}Fe x-rays can be obtained for a range of pressures and amplification fields, the highest gain obtained here being 3000 in 30 Torr with matching amplification fields of 24 500 V cm^{-1}. This is much improved over standard ThGEMs. The effect on energy resolution of varying the second amplification field revealed minima in the 30, 40 and 50 Torr data, suggesting further room for optimising the fields. Study of the second stage and some discrepancies found when extracting the Townsend parameters also suggested likely charge loss in the transfer region, described further in section 7.

7 Transfer field

Detailed now is characterisation and optimisation of the Transfer Field between meshes 2 and 3. This controls charge movement between the MM-ThGEM amplification stages, notable parameters being the charge transfer time and the factor by which this affects the overall gain. The field strength here is too low for electron multiplication but is vital to determining the efficiency of charge transfer, dictated mainly by losses from attachment to the hole walls and in transfer through the mesh planes. In electron drift gasses the ratio of field strength either side of a mesh is known to be correlated to its transparency to electrons [24]. However, for NI gases mesh losses are harder to characterise, mainly because electron attachment and detachment to ions is also occurring near the meshes. Regarding losses to the hole edges, this is expected to correlate with charge diffusion in the hole and, assuming no space charge and thermal diffusion, to be inversely proportional to the transfer field.

7.1 Effect of the transfer field on gas gain

Turning first to study how the transfer field affects the total MM-ThGEM gain in operation with SF_6, test of this were performed using ^{55}Fe with the same gas pressures as before and with collection and amplification fields set to nominal values, as detailed in table 3. Figure 16 shows the gain results obtained by measurement at mesh 4, vs. transfer field, with all other fields held constant.

2023 JINST 18 P08021

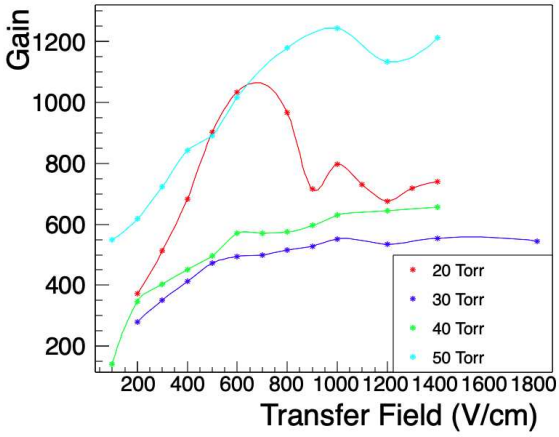

Figure 16. The gain vs transfer field in the MM-ThGEM.

Pressure (Torr)	**Cathode** (V)	V_{m1} (V)	**Amp 1** (V/cm)	**Amp 2** (V/cm)
20	500	140	22000	21500
30	500	140	23500	23500
40	600	150	26000	25500
50	600	150	28000	28000

Table 3. The field settings for each pressure when the transfer field is varied.

As seen in figure 16 the trend is for the gain to increase with transfer field asymptotically to a limit typically by 1000 V cm^{-1} beyond which there is no further increase. As no electron multiplication occurs in the transfer field, this increase can reasonably be attributed to a combination of improving charge extraction through mesh 2 and reduced losses to the hole edges. An exception is seen for 20 Torr where the gain decreases significantly after 600 V cm^{-1}. This behaviour at the lowest pressure is most likely attributed to onset ion feedback, to be discussed in section 8. Nevertheless, a general conclusion is that transfer fields of 600 V cm^{-1} to 1000 V cm^{-1} are likely optimal for minimising charge losses and maximising gain in the MM-ThGEM with low pressure SF_6.

7.2 Transfer times

Regarding charge transfer times between the amplification regions, this is expected to be mediated by negative ions and so will be significant, of order tens of microseconds, and thus particularly important to measure, for instance for understanding signal pulse shape. However, it also provides opportunity to measure the negative ion reduced mobility μ_0. This is feasible because the transfer time, $t_{m2\to m3}$ can be related to the transfer field, E_{transfer} and μ_0, by the equation

$$t_{m2\to m3} = \frac{d}{\mu_0 E_{\text{transfer}}} \frac{PT_0}{P_0 T} \tag{7.1}$$

where d is the transfer gap width, P the gas pressure, T the temperature, and P_0 and T_0 the pressure and temperature at STP. Making use of this relation the transfer times were first measured by recording coincident events in mesh 2 and 4 from exposure of the drift region to ^{241}Am alphas. The two amplification fields were set equal so that signals were approximately the same amplitude, the field values being 15 500 V cm^{-1}, 17 000 V cm^{-1} and 19 000 V cm^{-1} at 20, 30 and 40 Torr respectively. The amplification field is high enough that electrons should detach from the negative ions in the amplification regions so the extra contribution to the total travel time, and hence mobility, for charge transport between meshes 3 and 4 should be negligible, typically $O(10\,\text{ns})$. Figure 17 shows typical events at 30 Torr for 400 V cm^{-1} and 1700 V cm^{-1}.

As expected and seen in figure 17 the mesh 4 signal is delayed relative to mesh 2, the delay being shorter for the larger transfer field. Based on such data figure 18 shows full results for the transfer time

2023 JINST 18 P08021

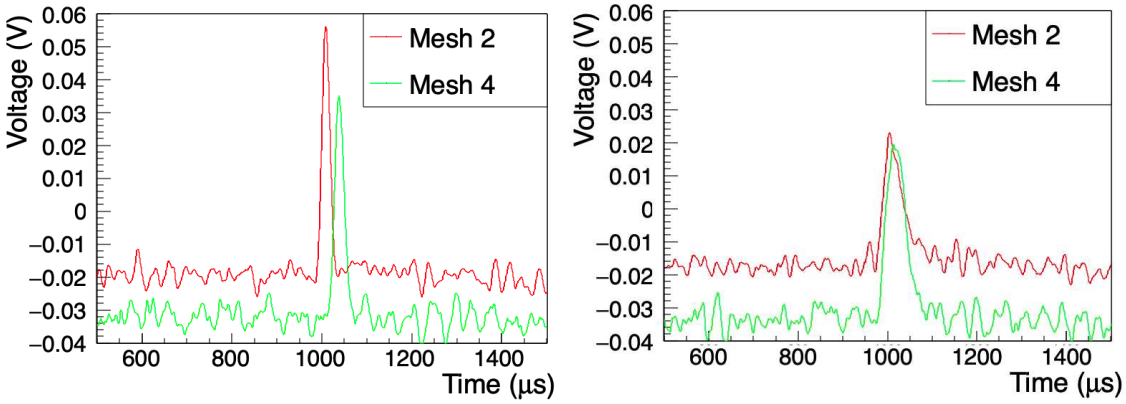

Figure 17. The alpha waveforms on meshes 2 and 4 for 30 Torr SF_6 with a 400 V cm^{-1} transfer field (left) and 1700 V cm^{-1} transfer field (right).

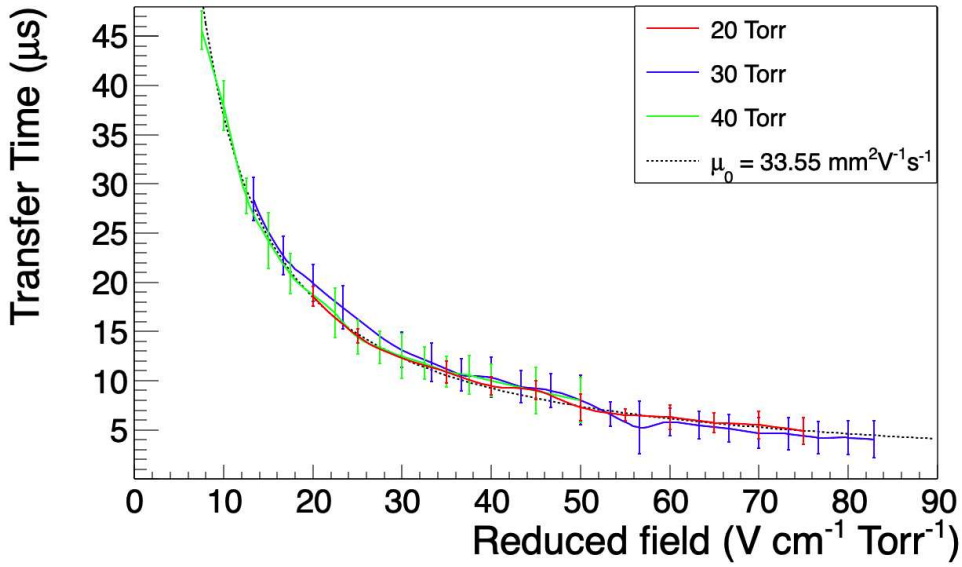

Figure 18. The transfer time from mesh 2 to mesh 4 in SF_6 against reduced drift field. Dotted line indicates the best fit to data (μ_0 = 33.55 mm^2/V/s).

against reduced transfer field at 20, 30 and 40 Torr. As illustrated by the fits shown the data is well described by equation (7.1) for all pressures, resulting in a measured reduced mobility of $\mu_0 = (33.6 \pm 0.5)$ mm^2/V/s. This is somewhat lower than previous measurements that put the mobility of SF_6^- ions at 53 mm^2/V/s with variation of order 5 mm^2/V/s between experiments [26]. Likely the explanation lies in the unique geometry of the MM-ThGEM measurement, notably the sensitivity to space-charge effects and the possibility that a substantial fraction of drifting charge are ions other than SF_6^-. Potential contributors to the production of ions other than SF_6^- might include outgassed contaminants in the detector, the short drift length and high charge density from the first amplification stage.

2023 JINST 18 P08021

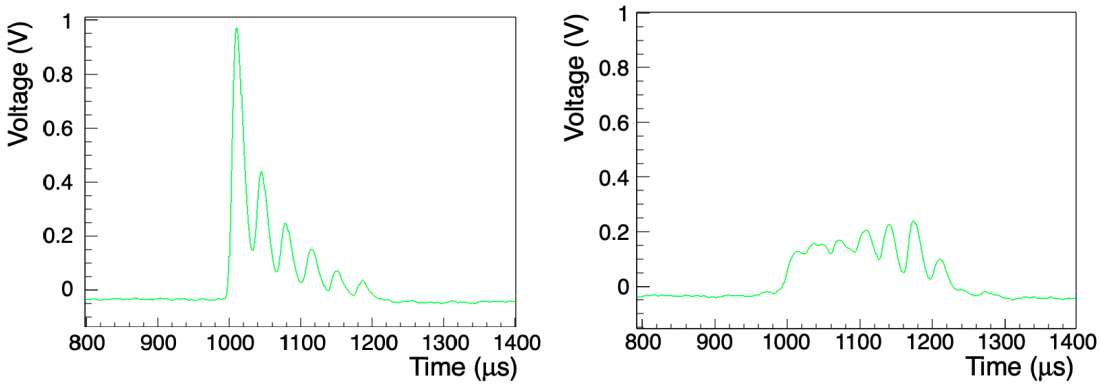

Figure 19. Sample ^{55}Fe events for 20 Torr SF_6 with 400 V cm^{-1} transfer field and 22 500 V cm^{-1} amplification fields, exhibiting the 'ringing' effect.

7.3 Conclusions

In summary, the measurements here demonstrate well that the transfer field's function to transport charge from the first amplification stage to the second amplification stage works as planned. Further optimisation is required but the preliminary work here suggests that minimising the impact on total gain with low pressure SF_6 requires transfer fields typically of 600 V cm^{-1} to 1000 V cm^{-1}.

8 Ion feedback effect in SF_6

During ^{55}Fe runs in low pressure SF_6 some signal "ringing" was observed characterised by peaks recurring for typically 200 µs, for instance as shown in figure 19. The tendency of electron recoils to create charge clusters means that multiple peak events are expected but not with the number and uniformity of peak separation observed here. The behaviour was only intermittently observed in 20 and 30 Torr, not higher pressures, suggesting a physical rather than electronic cause.

To investigate this a Fourier transform (FT) analysis was performed on a subset of waveforms, the aim being to separate any characteristic frequencies as a function of different pressures and drift, transfer, collection and amplification fields. The frequency spectrum was found to have a smooth exponential-like drop when no ringing was present, supplemented by localised peaks in frequency for runs that included ringing events. Figure 20 shows example results for 500 events revealing peaks centred at 28 kHz and 57 kHz. The former corresponds to period 36 µs, consistent with the peak separations observed in the best resolved individual events. The latter is likely the second harmonic of the first peak. In some runs the third harmonic was also observable.

From analysis of the heights and positions of the FT peaks the strength and frequency of the ringing was found to be independent of the drift and collection fields. However, correlations between frequency and the amplification and transfer fields were established as illustrated in figure 21. Here analysis shows the ringing frequency is proportional to the transfer field and inversely proportional to pressure.

The strength of the ringing, via the height of the first FT peak, was also found to be proportional to the amplification fields. At 20 Torr when both amplification fields were at or below 21 kV cm^{-1} the FT peak was not seen but for voltages larger than this the peak emerged, with magnitude

2023 JINST 18 P08021

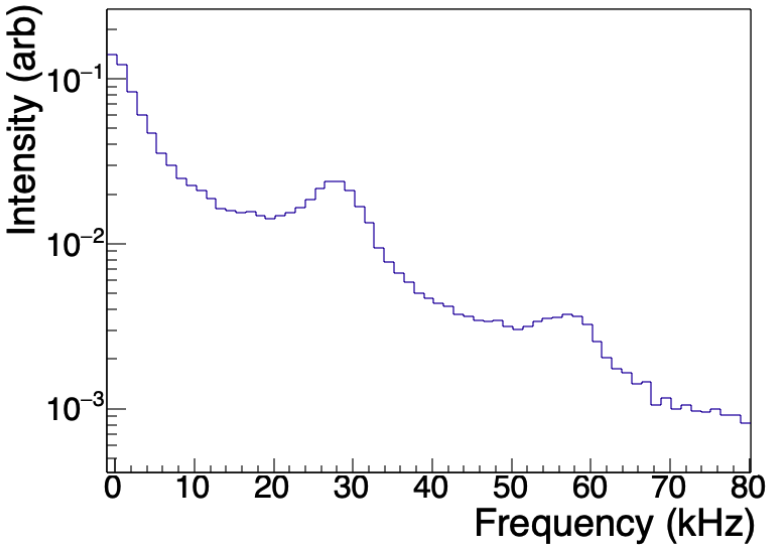

Figure 20. Fourier transform of 500 signal events in 20 Torr SF_6, 400 V cm^{-1} transfer field and 22 500 V cm^{-1} amplification fields.

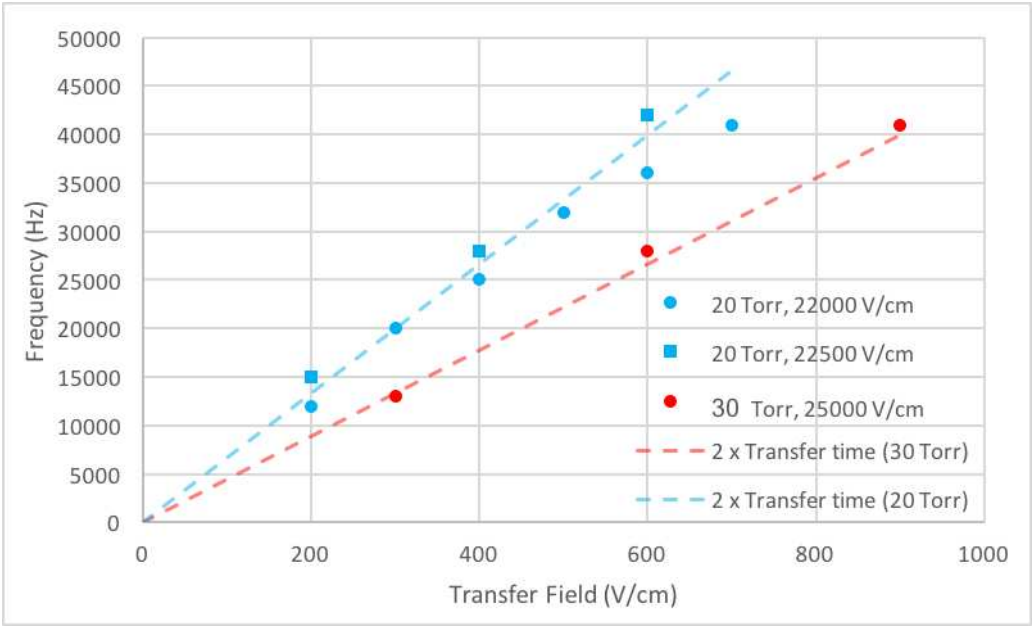

Figure 21. Average frequency of ringing determined by Fourier transform against transfer field for 20 and 30 Torr SF_6, amplification fields and pressures are indicated in the legend. The lines plotted are $\frac{1}{2t_{tr}}$ where t_{tr} is the transfer time calculated from the measured mobility, 33.6 mm^2/V/s.

proportional to the voltage. At 30 Torr the minimum amplification fields required to observe the effect was 24 kV cm^{-1} and at higher pressures the effect was not observed at any voltages. Also, as shown in figure 22, a further phenomena was observed at the highest amplification field used in 20 Torr SF_6 whereby the ringing increases in magnitude and then persists for an extended

2023 JINST 18 P08021

period. Fluctuations then continue between 0.5 V and the digitiser saturation at 1 V but with peaks continuing on the timescale of the ringing effect. In the example shown this continued until the device voltage was reduced. This suggests that the ringing effect is caused by a feedback process where the initial signal is, after a delay, reproduced with magnitude scaled by some factor. In the runaway state shown in figure 22, this factor exceeds one and the ringing gets increasingly large. The mechanism does appear to be self-limiting, and the signal does not appear to significantly exceed the ±1 V range of the digitiser.

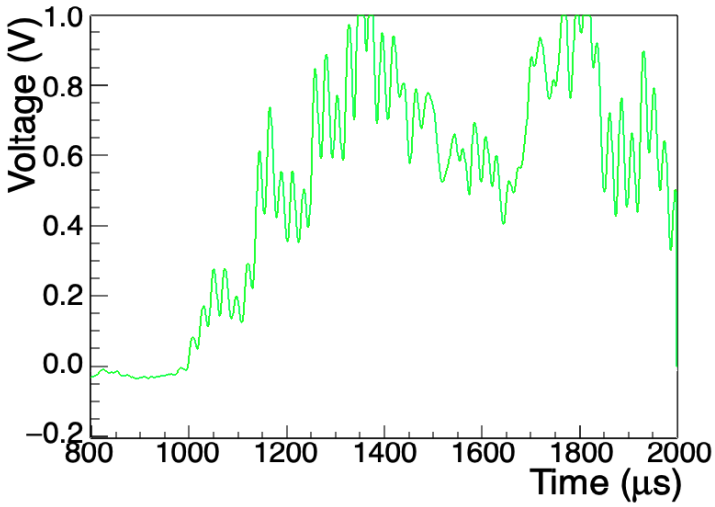

Figure 22. Onset of instability current 20 Torr SF_6 with 600 V cm^{-1} transfer field and 22 500 V cm^{-1} amplification fields.

Several potential mechanisms to explain the ringing phenomena and the relationships observed were considered, included feedback in the electronic amplification, secondary photo-ionisation, and the liberation of secondary electrons by backflowing positive ions. Electronic feedback could arise if the output of a part of the amplification chain were coupled to the input, the re-amplification of collected signal then resulting in feedback peaks following the initial signal arrival. However, the absence of ringing at higher pressure and the dependence on the transfer and amplification fields likely excludes this, and other mechanisms not reliant on charge transport in the gas. Regarding photo-ionisation, a known source of this in TPCs is scintillation photons produced during charge multiplication [27, 28]. In the MM-ThGEM such photons could be produced in the second avalanche field and potentially ionise electrons nearer the top of the hole, which would be transported back to the second amplification field and induce another avalanche. This would be consistent with the relationship between the amplification fields and the magnitude of the feedback observed. However, it is not consistent with rather slow time separation between peaks in the ringing events.

Turning to backflow of positive ions, this concept does appear well aligned with the data. Furthermore, a key supporting observation is that the ringing period found is close to twice that of the transfer time for negative ions in the transfer gap, as measured in section 7.2. It is known that the impact of positive ions on certain surfaces can produce ionised electrons [29]. In the MM-ThGEM positive ions formed in the second amplification field could propagate back through the transfer region and first amplification region, propelled there by the high field to impact on mesh

2023 JINST 18 P08021

1. The liberated electrons would then avalanche in the first amplification stage before travelling back through the transfer region to be multiplied again by the second amplification field. Here further production of positive ions would continue the cycle, the period then being equal to the time taken for the charge to make a round trip and the reproduction factor controlled by the amplification fields. The mobility of SF_6^+ ions is close to that of SF_6^-, consequently the time taken for backflowing positive ions to cross the transfer gap should be about the same as the transfer time of negative ions going the other way [26]. The fact that the effect was not observed for higher pressures could be attributed to the lower velocities of the positive ions in the first amplification field which would reduce the probability of electron emission from the first mesh.

The feedback effect results in significant distortion of the signal and likely also contributes to the anomalous measurements of the detector performance at 20 Torr discussed in sections 6 and 7. In order to mitigate these it is clear that care is needed to avoid operating the MM-ThGEM in regimes where significant distortions from the effect are present. At more than 30 Torr the effect is not a concern, and at 20 and 30 Torr care should be taken to avoid operating the device at high amplification fields. However, a positive aspect of the ion feedback is that it can be identified before runaway occurs and it appears not to cause discernible damage to the MM-ThGEM or electronics. This is in contrast to the violent sparking events which characterise the operational limit of ThGEMs.

9 Operation of the MM-ThGEM in CF_4:SF_6

Rather than using pure SF_6 it has been found that mixtures of CF_4 with small amounts of SF_6, typically with ratio around 14:1, has the advantage of preserving the negative ion drift properties of SF_6 while enhancing the fraction of minority charge carriers [30], which makes identification of minority peaks in the detector signal easier at low gains. A further advantage arises because SF_6 is a much more potent greenhouse gas than CF_4, so reducing the overall content is desirable, something particularly important for large detectors such as proposed by CYGNUS [9]. In this context some preliminary proof-of-principle tests of the MM-ThGEM were performed with CF_4:SF_6 mixtures. CF_4:SF_6 ratios of 30:2.2 Torr and 50:3.5 Torr were chosen for this for compatibility with previous work and the same vessel, instrumentation and bias scheme was used as described in section 3. For all runs the first mesh and cathode biases were set to 140 V and −500 V respectively and the first amplification field to 20 500 V cm^{-1} for the 30:2.2 Torr runs and 24 500 V cm^{-1} for the 50:3.5 Torr runs. Figure 23a shows example results for the total gain against transfer field with the second amplification field set to 20 500 V cm^{-1} and 24 000 V cm^{-1} for the 30 Torr and 50 Torr CF_4 runs respectively. Figure 23b shows the gain against the second amplification field with the transfer field fixed at 600 V cm^{-1}. Note that for the short drift distance used, the different species of charge carrier in the gas do not have time to separate and so all the event signal is contained in a single peak.

As indicated by figure 23a and 23b reliable and stable operation of the MM-ThGEM was found to be straightforward with the CF_4:SF_6 mixtures which show significant promise. Comparing the results with, for instance, figure 13, it is evident that the amplification field required to achieve a given gain is significantly lower in CF_4:SF_6 than in pure SF_6. For example, the gain for matching amplification fields of 20 500 V cm^{-1} in 30:2.2 Torr CF_4:SF_6 is 370 whereas an equivalent gain in 30 Torr of pure SF_6 requires amplification fields of ≈22 300 V cm^{-1}. The overall trend is for the gain to increase with increasing amplification field, although the relationship does not appear to be exponential as might be expected. The change in gain with transfer field follows the same general shape as in pure SF_6, tending to plateau off at high transfer fields.

2023 JINST 18 P08021

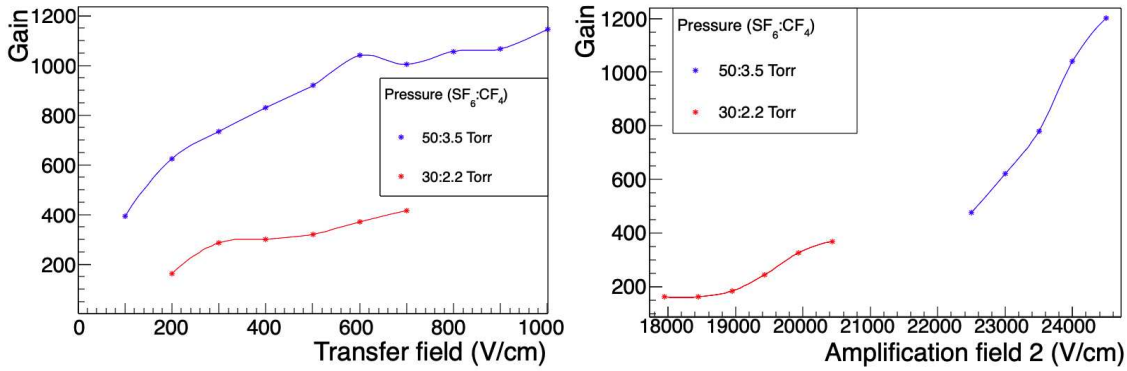

(a) Gas gain against transfer field.

(b) Gas gain against second amplification field.

Figure 23. Variation in the gain with transfer field and second amplification field for the MM-ThGEM in CF_4:SF_6 mixtures at 30:2.2 Torr and 50:3.5 Torr.

10 Conclusions

This work outlines successful operation of the Multi-Mesh ThGEM (MM-ThGEM) device in a negative ion (NI) gas at low pressure for the first time. The device, comprising a collection region and two amplification regions was initially operated in low pressure CF_4. This highlighted the importance of the collection field stage. Subsequent simulations of electron transport demonstrated a number of competing processes occur during charge transport through the device. Moving to SF_6 considerably altered the dynamics of the charge transport, but a range of collection fields were shown to be sufficient to collect the majority of the charge, consistent with simulation of ion drift in the gas. Studies with different amplification fields then showed reliable and stable operation and enabled estimation of the Townsend parameters of SF_6. It was demonstrated that gains in excess of 1000 were achievable with little tuning.

Study of charge transfer in the gap between avalanche regions confirmed the negative ion behaviour with SF_6 and enabled a measurement of the reduced mobility of negative ions in the gap of $\mu_0 = (33.6 \pm 0.5)\ \mathrm{mm}^2/\mathrm{V/s}$. This indicated the presence of more complex effects occurring in the gap than expected. A gradual increase in gain with increasing transfer field led to optimisation of the field at about $1000\ \mathrm{V\,cm}^{-1}$. The device was found to be more stable than typical ThGEMs, with none of the damaging sparks which are observed at the ThGEM operating point in SF_6. At 20 and 30 Torr the device's failure mode was a ringing effect identified as positive ion feedback, while this had a distorting effect on signals at high amplification fields it was not destructive to the MM-ThGEM or electronics. A further gas mixture, CF_4:SF_6 was also tentatively explored and demonstrated promise with significantly higher gains than were observed in SF_6 alone for similar pressures and field values.

Acknowledgments

The authors would like to acknowledge support for this work from AWE, the CERN MPGD group and a University PhD scholarship award to C. Eldridge.

2023 JINST 18 P08021

References

[1] R. de Olivera and M. Cortesi, *First performance evaluation of a multi-layer thick gaseous electron multiplier with in-built electrode meshes — MM-THGEM*, 2018 *JINST* **13** P06019 [arXiv:1804.04643] [INSPIRE].

[2] J.L. Feng, *Dark matter candidates from particle physics and methods of detection*, *Ann. Rev. Astron. Astrophys.* **48** (2010) 495 [arXiv:1003.0904] [INSPIRE].

[3] XENON collaboration, *Light Dark Matter Search with Ionization Signals in XENON1T*, *Phys. Rev. Lett.* **123** (2019) 251801 [arXiv:1907.11485] [INSPIRE].

[4] R. Bernabei et al., *First model independent results from DAMA/LIBRA-phase2*, *Nucl. Phys. Atom. Energy* **19** (2018) 307 [arXiv:1805.10486] [INSPIRE].

[5] LZ collaboration, *First dark matter search results from the LUX-ZEPLIN (LZ) experiment*, arXiv:2207.03764 [INSPIRE].

[6] COSINE-100 collaboration, *Search for a dark matter-induced annual modulation signal in NaI(Tl) with the COSINE-100 experiment*, *Phys. Rev. Lett.* **123** (2019) 031302 [arXiv:1903.10098] [INSPIRE].

[7] G.J. Alner et al., *The DRIFT-II dark matter detector: design and commissioning*, *Nucl. Instrum. Meth. A* **555** (2005) 173 [INSPIRE].

[8] DRIFT collaboration, *Improved sensitivity of the DRIFT-IId directional dark matter experiment using machine learning*, *JCAP* **07** (2021) 014 [arXiv:2103.06702] [INSPIRE].

[9] S.E. Vahsen et al., *CYGNUS: feasibility of a nuclear recoil observatory with directional sensitivity to dark matter and neutrinos*, arXiv:2008.12587 [INSPIRE].

[10] DRIFT collaboration, *First background-free limit from a directional dark matter experiment: results from a fully fiducialised DRIFT detector*, *Phys. Dark Univ.* **9-10** (2015) 1 [arXiv:1410.7821] [INSPIRE].

[11] N.S. Phan et al., *The novel properties of SF_6 for directional dark matter experiments*, 2017 *JINST* **12** P02012 [arXiv:1609.05249] [INSPIRE].

[12] C.K. Shalem et al., *Advances in thick GEM-like gaseous electron multipliers. Part II: low-pressure operation*, *Nucl. Instrum. Meth. A* **558** (2006) 468 [physics/0601119] [INSPIRE].

[13] M. Alexeev et al., *Development of THGEM-based photon detectors for COMPASS RICH-1*, *Phys. Procedia* **37** (2012) 781 [INSPIRE].

[14] L. Arazi et al., *THGEM-based detectors for sampling elements in DHCAL: laboratory and beam evaluation*, 2012 *JINST* **7** C05011 [arXiv:1112.1915] [INSPIRE].

[15] Cremat Inc, *CR-150-R5 evaluation board: application guide*, https://www.cremat.com/CR-150-R5.pdf.

[16] G.F. Reinking, L.G. Christophorou and S.R. Hunter, *Studies of total ionization in gases/mixtures of interest to pulsed power applications*, *J. Appl. Phys.* **60** (1986) 499.

[17] ORTEC, 926-*M32-USB multichannel analyzer: specification sheet*, (2009).

[18] S.R. Hunter, J.G. Carter and L.G. Christophorou, *Electron attachment and ionization processes in CF_4, C_2F_6, C_3F_8, and n-C_4F_1*, *J. Chem. Phys.* **86** (1987) 693.

[19] M. Pitt et al., *Measurements of charging-up processes in THGEM-based particle detectors*, 2018 *JINST* **13** P03009 [arXiv:1801.00533] [INSPIRE].

2023 JINST 18 P08021

[20] I. Lopes, H. Hilmert and W.F. Schmidt, *Ionisation of gaseous and liquid sulphur hexafluoride by ^{60}Co γ-radiation*, *J. Phys. D* **19** (1986) L107.

[21] F.J. Iguaz, E. Ferrer-Ribas, A. Giganon and I. Giomataris, *Characterization of microbulk detectors in argon- and neon-based mixtures*, 2012 *JINST* **7** P04007 [arXiv:1201.3012] [INSPIRE].

[22] P.K. Lightfoot et al., *First operation of bulk micromegas in low pressure negative ion drift gas mixtures for dark matter searches*, *Astropart. Phys.* **27** (2007) 490 [INSPIRE].

[23] B. Chan, *High-level quantum chemistry reference heats of formation for a large set of C, H, N, and O species in the NIST chemistry webbook and the identification and validation of reliable protocols for their rapid computation*, *J. Phys. Chem. A* **126** (2022) 4981.

[24] K. Nikolopoulos, P. Bhattacharya, V. Chernyatin and R. Veenhof, *Electron transparency of a micromegas mesh*, 2011 *JINST* **6** P06011 [arXiv:2005.01065] [INSPIRE].

[25] Fast ComTec, *CR*-200 *Gaussian shaping amplifier (rev.* 2*): application guide*, https://www.fastcomtec.com/fwww/datashee/amp/cr-200.pdf.

[26] R. Morrow, *A survey of the electron and ion transport properties of SF_6*, *IEEE Trans. Plasma Sci.* **14** (1986) 234.

[27] P.J. Campion, *Spurious pulses in proportional counters*, *Nucl. Instrum. Meth.* **112** (1973) 75.

[28] G.W. Penney, S.F. Nygren and R.E. Voshall, *Photoionization as the secondary mechanism in a Townsend breakdown*, *IEEE Trans. Commun. Electron.* **83** (1964) 203.

[29] H. Genz, D.S. Harmer and R.W. Fink, *Measurement by two-dimensional pulse analysis of the time and energy distributions of afterpulses in proportional counters*, *Nucl. Instrum. Meth.* **60** (1968) 195.

[30] R.J. Lafler, *Studying the properties of SF_6 gas mixtures for directional dark matter detection*, Ph.D. thesis, University of New Mexico, Albuquerque, NM, U.S.A. (2019).

2023 JINST 18 P08021